RSC Advances

COMMUNICATION

View Article Online
View Journal | View Issue

Cite this: *RSC Adv.*, 2016, **6**, 17360

Received 3rd August 2015
Accepted 1st February 2016

DOI: 10.1039/c5ra15490a

www.rsc.org/advances

Effect of crystallographic orientation on the tribological behavior of electrodeposited Zn coatings

K. R. Sriraman,† P. Manimunda,† R. R. Chromik* and S. Yue

Electrodeposited Zn coatings are used in the automotive and aerospace industries for the cathodic protection of high-strength steel fasteners and components. These coatings are polycrystalline and exhibit preferred orientation depending on the deposition parameters. They undergo varying amounts of contact stress during use and this requires an understanding of the effect of the crystallographic orientation of the coatings on their friction and wear behaviors. In this study, Zn coatings with different orientations were electrodeposited on low-carbon steel substrates by modifying the plating conditions. A reciprocating pin on a disk tribometer with a steel counter sphere under a constant normal load was used to help understand the effect of the orientation of the coating on the coefficient of friction and the sliding behavior of the coatings. *Ex situ* analysis of the tribo/transfer films was performed using X-ray diffraction, nanoindentation, Raman spectrometry, electron microscopy and nanoindentation techniques. The crystallographic orientation of the coating-tribo/transfer film was correlated with the tribological behavior, strain hardening, and third body formation under contact conditions.

Introduction

The electrodeposition of Zn has been widely used for the past two centuries for the galvanic protection of steel from corrosion. Various bath chemistries of Zn have been utilized to generate coatings, namely alkaline cyanide baths, acid chloride baths, and non-cyanide alkaline baths. These bath chemistries give rise to field-oriented whisker-type coatings, field-oriented coherent-type deposits with grain sizes that are constant throughout the deposit thickness, and unoriented dispersed-type crystals with well-distributed grain sizes.[1] Rack-and-barrel plating processes use alkaline non-cyanide baths and acid chloride baths; toxic cyanide baths have become obsolete as a result of environmental regulations.[1] If there is a lack of conforming electrodes, preferred orientation effects on the coating may occur in recesses when plating large and intricate components, such as the outer cylinder of the landing gear of an aircraft, by rack-plating processes. This could lead to anisotropy in the wear and corrosion resistance of coatings. The texture of the deposit depends on the plating conditions, such as the bath chemistry, the current density, the pH of the plating bath, the additives, the orientation of the substrate grain, and the nature of the finish of the substrate surface. Tomov *et al.*[2] investigated the evolution of texture in Zn deposits from a plating bath based on Zn chloride. The texture of the coatings depended on the inhibitors added to the bath. The bath without inhibitors produced random orientations on the Zn coatings, whereas the baths with additives resulted in coatings with strong (110) and (100) orientations. The crystallographic orientation of the coatings produced from plating baths was also dependent on the orientation of the substrates – in this instance Cu and Ni.[2] Mouanga *et al.*[3,4] reported that, in a chloride-based plating bath, the additives coumerin and thiourea changed the orientation of the deposit from (112) to a strong (110). They also reported that the additives guandin and urea had no effect on the crystallographic reorientation of the deposits.[4]

Raeissi and co-workers[5–8] investigated the evolution of texture in Zn-based coatings produced from a Zn sulfate bath while evaluating all the electrodeposition parameters. They reported that the texture of the Zn electrodeposits greatly depended on the nucleation and growth mechanisms. Strong γ fibers on the cold-rolled annealed steel substrate promoted the evolution of texture components without fibers.[5] A higher overvoltage on the electrode surface, which was achieved by increasing the current density, increased the intensity of the basal plane.[6] A finer substrate finish promoted a mixed orientation of textures on the coating, *i.e.* basal fibers and non-fiber pyramidal plane orientations of (115) or (116).[6] A mechanically polished surface yielded a weak (115) and (116) fiber texture and the basal plane texture completely disappeared. Some pyramidal components of the (101) and (102) planes were observed to a lesser extent.[8]

Department of Mining & Materials Engineering, McGill University, Montreal, Qc H3A 2B2, Canada. E-mail: richard.chromik@mcgill.ca

† Denotes equal contribution as first authors.

Zn coatings are used for corrosion protection on threaded fasteners in different applications.[9] The aerospace industry has used Cd over several decades for the galvanic protection of steel. However, as Cd is toxic, its use has been restricted, which has led to development of various Zn-based alternatives. The leading candidate among the alternatives is a Zn–Ni alloy. Although there has been much documented research on the properties of Zn–Ni alloys,[10–12] there is little published work on the effect of orientation on the properties of Zn-based coatings. Li and co-workers have studied the deposition parameters,[13] corrosion behavior,[14] and tribological behavior[15] of nanocrystalline Zn coatings using pulsed electrodeposition methods. However, although Li *et al.*[15] studied the wear behavior of electrodeposited Zn, the focus of their work was mainly the effect of grain refinement on the mechanical properties and wear behavior, rather than the crystallographic orientation. There is also considerable interest in the development of Zn–Co and Zn–Fe deposits as potential replacements for Cd.[16,17] To evaluate Zn-based alloy coatings as replacements for Cd, a thorough understanding of the properties of the baseline coating (metallic Zn) is required. Zn is a soft metal and does not show significant wear resistance compared with harder coatings such as electroless Ni. For softer coatings applied on threaded fasteners, the tribological behavior, such as the transfer and tribo-film rheology,[10] is important during torquing and removal/reinstallation of the fastener. The plating industry uses a plating solution based on acid chloride for the majority of applications rather than a sulfate-based plating bath because chloride ions are easier to handle and dispose of than sulfate ions. However, there is no fundamental understanding of why different orientations of Zn show different behaviors in industrial applications.

The work reported here investigated the role of coating texture and orientation on the tribology of electrodeposited Zn coatings obtained from two different bath chemistries. The friction and wear behavior of the coatings was correlated with the evolution of the tribo-transfer film using X-ray diffraction, electron microscopy, and indentation and spectrochemical analyses.

Experimental methods

Coating deposition

Two different plating baths were chosen to obtain Zn coatings with different orientations/textures: a $ZnCl_2$-based plating bath and a $ZnSO_4$-based bath. A general purpose low-carbon steel sheet of SAE 1008 grade steel was used as the substrate material. The substrate was prepared with SiC abrasive grinding paper using 600 and 800 grit finishes and then fine-polished with a 0.05 μm colloidal SiO_2 suspension. The substrate was then acid-pickled in a 10% HCl solution for the chloride bath and a 10% H_2SO_4 solution for the sulfate plating bath before electrodeposition of the coating. Table 1 gives the bath chemistry and plating parameters. An EG&G PAR Model 363 potentiostat/galvanostat was used to electrodeposit the coating in the galvanostatic mode in a two-electrode system.

Table 1 Bath chemistry and plating parameters for electrodeposition of Zn

Chloride bath		Sulfate bath	
Chemistry	Concentration (g L^{-1})	Chemistry	Concentration (g L^{-1})
$ZnCl_2$	60	$ZnSO_4$	620
KCl	250	Na_2SO_4	72
H_3BO_3	25	H_2SO_4	<10
HCl	<1		
Other plating parameters			
Chloride bath			Sulfate bath
Current density (mA cm^{-2})		5	10
pH		4.2	2
Plating time (h)		3	1.5
Coating thickness (μm)		20–25	20–25

The deposition was carried out in a glass beaker with pure metallic Zn as a counter electrode to give a constant coating thickness of 20–25 μm.

Tribology tests

Wear tests were performed with reciprocating motion using a custom-built reciprocating ball on a disk tribometer.[18,19] A hardened AISI 440C grade stainless-steel ball (6.35 mm diameter) was used as the slider against the coating with a 3.98 N force; the initial maximum Hertzian contact pressure was 750 MPa. The tests were conducted at a sliding velocity of 14 mm S^{-1} and the track length was 20 mm. The maximum number of sliding cycles was 2000, resulting in a total sliding distance of 46.54 m. The friction was monitored throughout each test using a piezoelectric transducer, which sampled the lateral forces at a rate of 2000 Hz. An average friction coefficient was calculated for each friction cycle using the central region of each track in the calculation. Data near the turn-around points at ~1% of the track length were omitted from this calculation. To generate the wear data at different intervals in the sliding cycle, separate 20 mm length tracks were obtained at 10, 50, 100, 200, 500, 850, 1200, and 2000 cycles. These tracks were used for *ex situ* mechanical and textural analyses.

We also investigated the chemical changes associated with sliding. For chemical analysis, it is mandatory to generate wear tracks under similar laboratory conditions (humidity and temperature). A stripe test was performed in which tracks corresponding to 10, 75, 200, 500, 850, and 2000 sliding cycles were generated in a single test and used for chemical analysis. A stripe test is a wear test in which an initial track length of 20 mm is reduced by 2 mm per time after a certain number of cycles.[20] This results in one single wear track with sections corresponding to different sliding distances. This method facilitates the rapid estimation of physicochemical changes during a wear test and helps to identify the areas of interest that may need more detailed examination.[20]

Characterization

Wear track morphology, crystallography, and the elemental and chemical composition of the coatings were studied using scanning electron microscopy (SEM), X-ray diffraction and Raman spectrometry. An FEI Inspect F50 field-emission gun scanning electron microscope coupled with energy-dispersive spectrometry (EDS) was used to observe the surface and cross-sectional morphologies, tribo/transfer films, and wear track morphologies of the coatings. The coating thickness was estimated using both the weight gain method and by microscopy of the cross-sections. The coating and tribo film textures were measured using a Bruker Discover D8-HISTAR 2D area detector diffractometer with Co Kα radiation and a 0.8 mm collimated X-ray beam in a standard θ–2θ configuration. The pole figures were measured in the goniometer by simultaneously measuring all three (002), (100), and (101) reflections of Zn in one measuring frame and then integrating the results using Bruker Multex software. These raw pole figures were subsequently used to calculate the orientation distribution function and were normalized based on the orientation distribution function using TexTools software. The chemical composition of the wear track and the debris were analyzed using an InVia Raman microscope (Renishaw, UK). The excitation source was a 514.5 nm Ar + laser. Neutral density filters were used during spectral acquisition to decrease the laser power to 5 mW to avoid damaging the sample. The Raman-scattered light was collected in a backscattering geometry using a Leica 50× objective lens and then dispersed using a grating with 1800 lines per mm. The resolution of the spectrometer was 1 cm^{-1} and the spectral acquisition time was fixed to 10 s.

The hardness, H, and reduced modulus, E^*, of the coatings and transfer film were determined using an instrumented nanoindentation technique (Triboindentor, Hysitron, USA). The force and displacement sensitivity of the instrument were <30 nN and <0.2 nm, respectively. A diamond Berkovich tip (tip radius ~100 nm) was used for the indentation test. The indentation experiments were performed in the load control mode with peak loads varying from 40 μN to 1 mN. The load

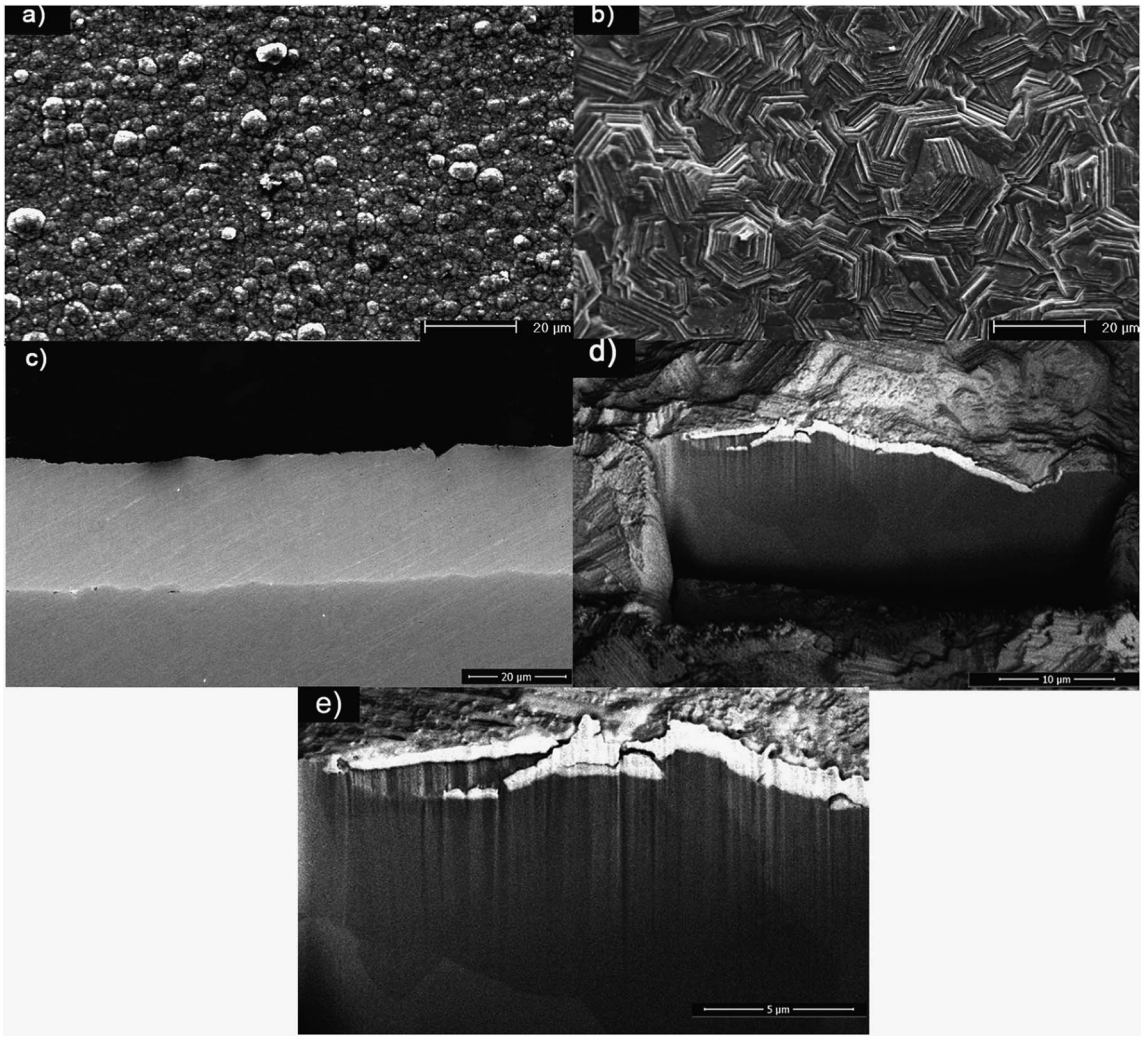

Fig. 1 (a) Surface morphology of Zn from the chloride bath. (b) Surface morphology of Zn from sulfate bath. (c) Metallographic cross-sectional morphology of Zn from the chloride bath. (d, e) Focused ion beam trench-cut cross-section of Zn from the sulfate bath.

displacement curves were fitted using the Oliver–Pharr method.[21,22]

Results and discussion

Coating characteristics

Fig. 1a and b show the surface morphologies of the coatings deposited from two different plating solutions. The morphology of the Zn coating obtained from the $ZnCl_2$ bath shows the most commonly observed cauliflower-type morphology (Fig. 1a).[23] The platelet size ranged from 2 to 5 μm. The Zn coatings obtained from the sulfate bath consisted of clusters of individual hexagonal platelets (Fig. 1b), typical of Zn coatings deposited from mechanically finished substrate surfaces.[8]

Fig. 1c–e show the cross-sectional morphologies of the coatings. The coatings obtained from the chloride bath showed a uniform dense interface as a result of the spherical morphology of the coating, which enabled close packing of the platelets. The coatings obtained from the sulfate bath were hexagonal platelets bunched over each other and hence the surface coverage was not uniform, resulting in a higher surface roughness. The preparation of the cross-sections of these coatings by metallographic methods resulted in artifacts due to the platelets being pulled out during polishing. A focused ion beam rectangular trench (15 μm in depth) was therefore cut from the surface. The observed cross-section of the coating was uniform with well-defined grains along the thickness.

Fig. 2 shows the pole figure of the distribution of crystallographic orientations for the Zn coatings obtained from the chloride bath. These coatings exhibited a stronger (100) fiber texture (Fig. 2b), *i.e.* the (100) planes were oriented in the normal direction perpendicular to the frame of reference or in the *Z* direction. The other two reference directions were the rolling direction and the transverse direction. Weak (101) fibers and an absence of basal fibers can be observed from Fig. 2a and c.[2] The inverse pole figure in Fig. 2d shows that this coating also exhibited a weak pyramidal plane (110) and a strong prism plane orientation (100). The presence of (100) and (110) textures on the coatings deposited from the chloride bath was a result of the lower overvoltage and also the presence of Zn hydroxide ions near the cathode surface, which caused an auto-inhibitor effect in the absence of additives.[2] This coating is referred to throughout this paper as $Zn_{(100)}$.

Fig. 3 shows the pole figure of Zn coatings deposited from the sulfate bath. This coating showed a very strong basal plane fiber, *i.e.* all the basal planes were oriented in the normal direction of the reference frame. The inverse pole figure in Fig. 3d also shows an absence of pyramidal or prismatic plane reflections and only basal plane intensities populating the map.

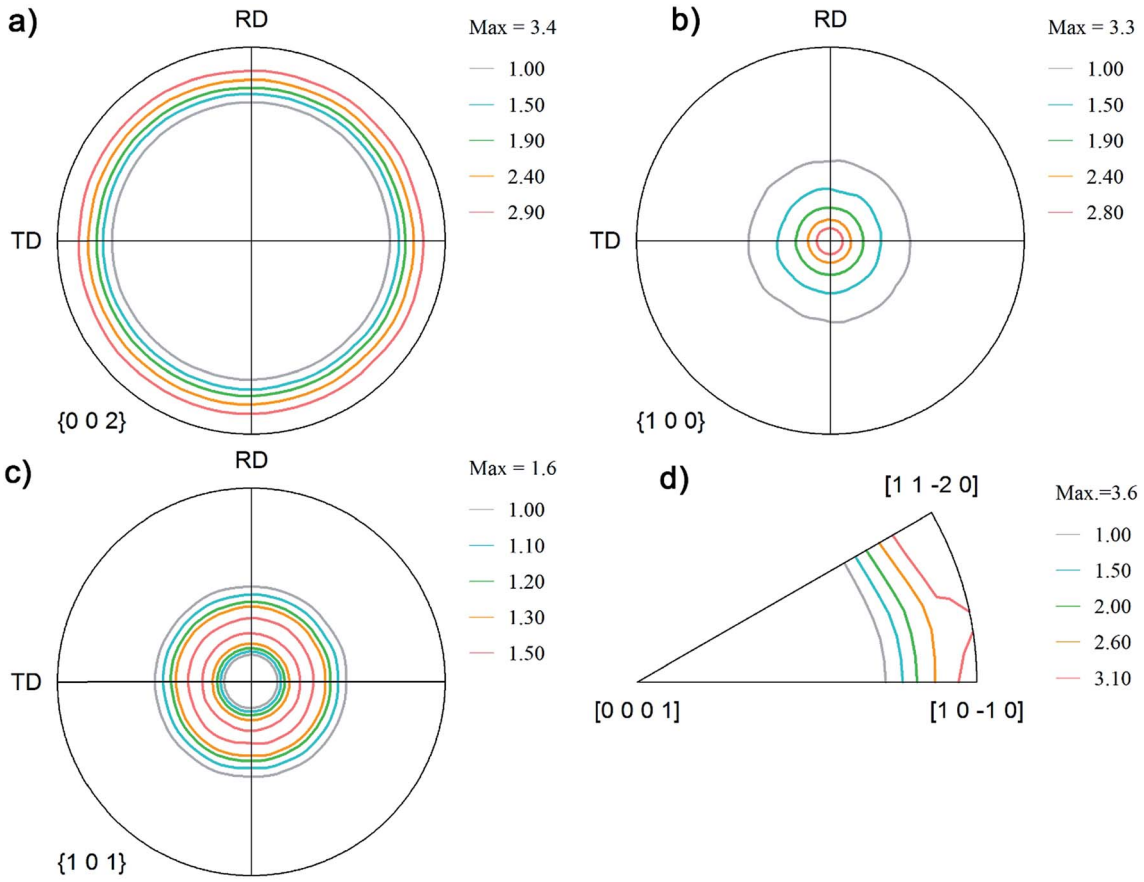

Fig. 2 Pole figure notation of the orientations on the coatings obtained from the chloride plating bath: (a) (002); (b) (100); (c) (101); and (d) inverse pole figures.

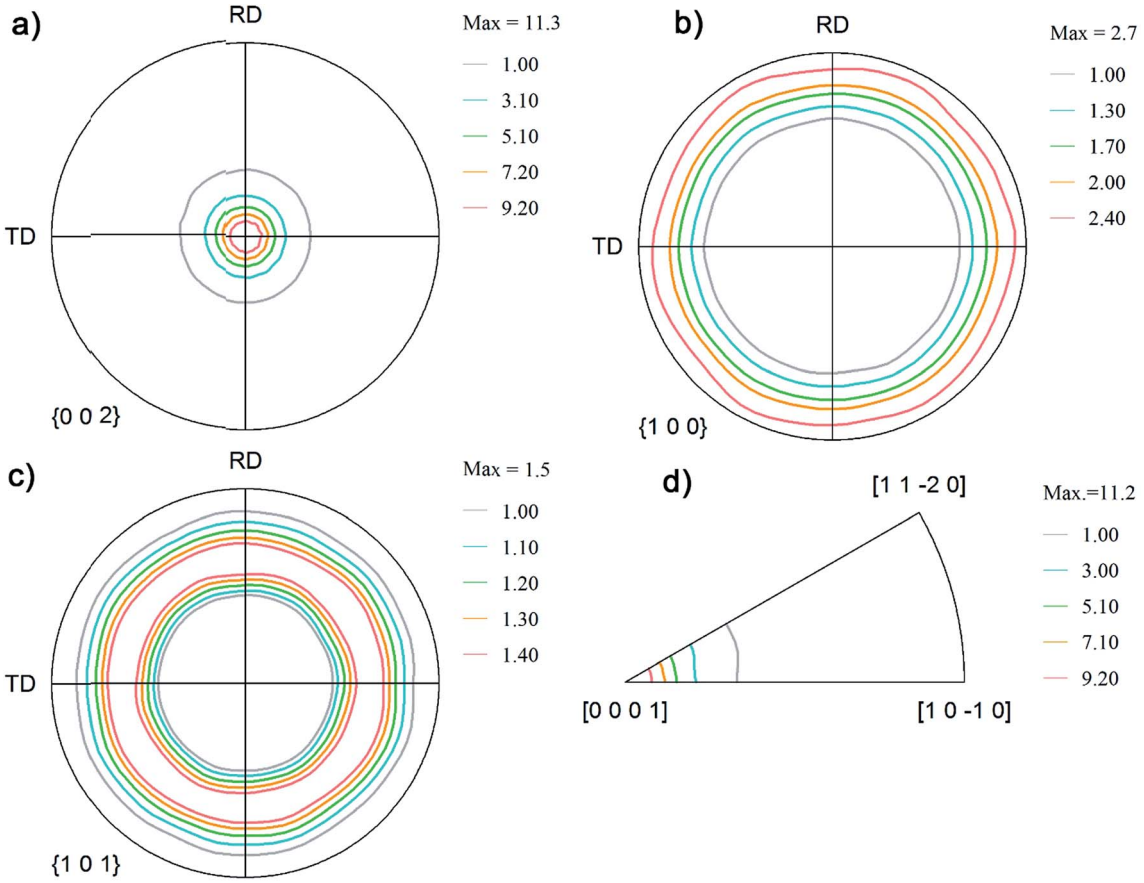

Fig. 3 Pole figure notation of the orientations on the coatings obtained from the sulfate plating bath: (a) (002); (b) (100); (c) (101); and (d) inverse pole figures.

The pole figure observations from both the coatings corroborate observations from the surface morphology. The Zn coatings from the chloride bath had randomly distributed spheroidal plates, whereas the basal plates in the coatings obtained from the sulfate bath were stacked vertically, *i.e.* aligned toward the normal plane. Coatings from the sulfate bath exhibited a strong basal plane orientation as a result of the higher overvoltage related to the higher current density and faster nucleation of the grains than those in the chloride bath.[6,7] This coating is referred to as $Zn_{(002)}$.

Fig. 4 shows the mechanical properties of the coatings measured using the nanoindentation method. The roughness values (R_a) of the as-plated $Zn_{(100)}$ and $Zn_{(002)}$ samples were 0.7 and 5 μm, respectively. The surface roughness was reduced by grinding with a fine 4000 grit SiC paper, followed by chemico-mechanical polishing in an alcohol-based Al_2O_3 suspension (50 nm particle size). Polished coatings with a surface roughness of 30–100 nm were used for the indentation tests.

The average hardness of the basal plane oriented coating (sulfate bath, $Zn_{(002)}$) was 0.63 GPa and for the prism plane coating ($Zn_{(100)}$) 1.02 GPa. Both coatings showed a different measured modulus. The measured modulus for the $Zn_{(002)}$ coating was 69 GPa, whereas the $Zn_{(100)}$ coating had a modulus of 110 GPa. The measured mechanical property data suggested a strong dependency on the coating orientation. For the $Zn_{(002)}$ coating, the majority of the basal planes were parallel to the substrate. When indentation was performed on the basal plane, the larger c/a ratio[24] (1.856) of Zn resulted in a lower modulus. In addition to the orientation, the lower compactness (Fig. 1b) resulted in inferior mechanical properties.

Friction and wear behavior

Fig. 5a shows the friction force evolution with respect to the number of sliding cycles for the coatings at 750 MPa initial Hertzian contact pressure.

The friction traces showed distinct regimes for both coatings: a prolonged running-in period (up to 500 cycles) followed by unsteady or reduced friction (500–800 cycles) and a steady-state regime (800–2000 cycles). During the running-in period (first 10 cycles), the coefficient of friction (COF) for the $Zn_{(100)}$ coating increased to 0.8 from an initial value of 0.3. The friction coefficient then stabilized until 500 cycles and then dropped to 0.4. The COF increased again to 0.6 at 600 cycles and dropped off to 0.4 at 800 cycles, after which it stabilized to a value of 0.45 until the end of the wear test. For the $Zn_{(002)}$ coating, the COF increased to a lower value of 0.6 from 0.3 within the initial 10 cycles. A decrease in the COF was observed at 200 cycles and it then again increased to 0.6

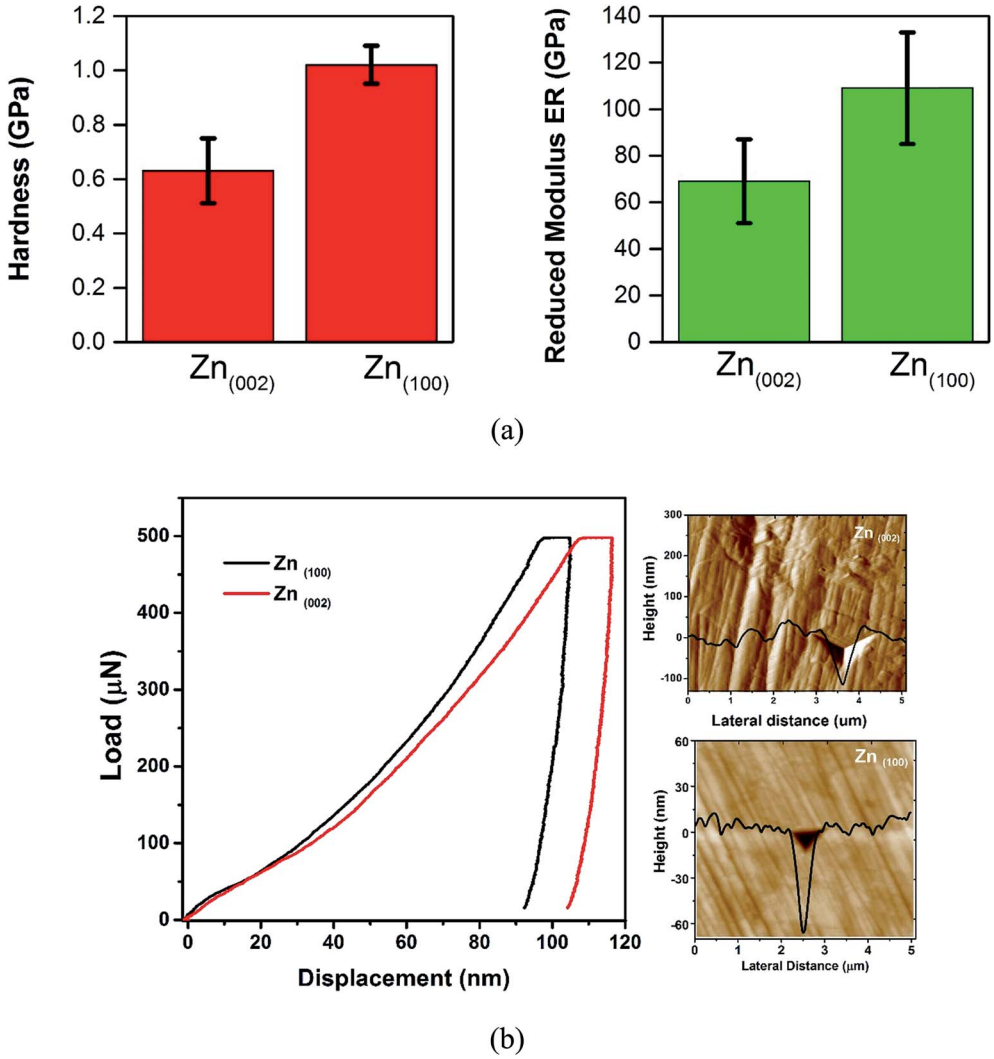

Fig. 4 (a) Hardness and reduced modulus (E_R) of the coatings. (b) Typical load displacement curves and SPM images of the indents.

at 250 cycles. The friction coefficient started to slowly decrease from 400 to 750 cycles from 0.6 to 0.45, and then became stable until the end of the test.

Fig. 5b shows the variation in the wear volume as a function of sliding distance. The wear volume of the $Zn_{(100)}$ coating was lower than that of the $Zn_{(002)}$ coating. The primary reason for the

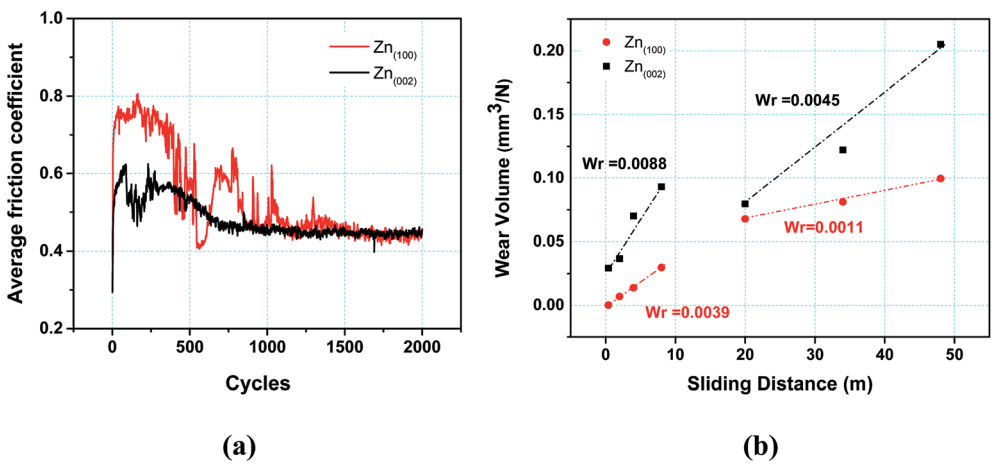

Fig. 5 (a) Variation in average friction coefficient *versus* number of cycles. (b) Variation in wear volume *versus* sliding distance.

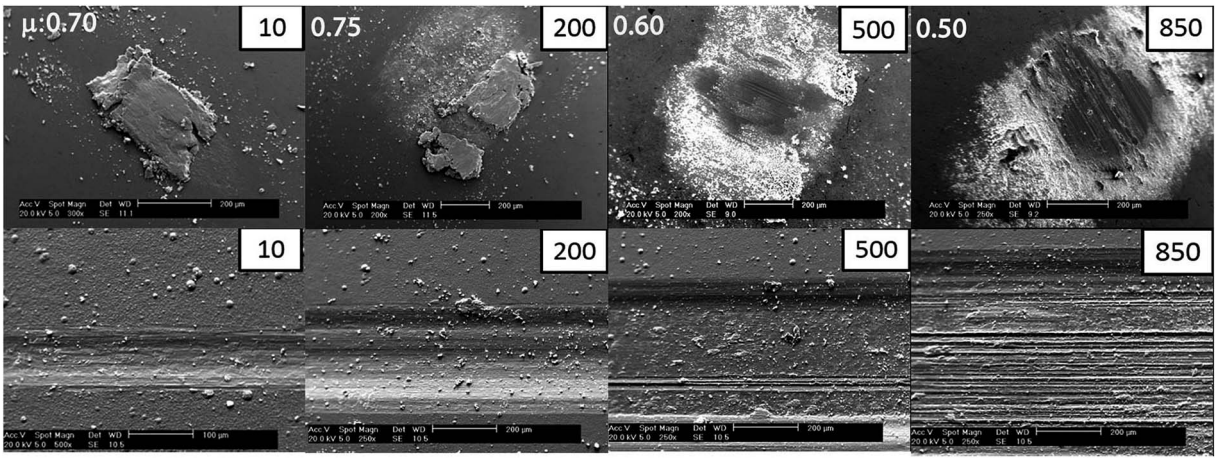

Fig. 6 *Ex situ* SEM micrographs of the counterface (top) and wear track (bottom) of $Zn_{(100)}$ coatings.

lower wear of the (100) coating was its higher mechanical properties (Fig. 4). Both coatings also showed two distinct wear regimes (Fig. 5b). A higher wear was observed for <10 m of sliding. This was followed by a steady-state period with a lower wear for >10 m of sliding. Although the wear rates decreased for both coatings after 10 m sliding distance, the wear rate (88×10^{-4} mm^3 N^{-1} m^{-1}) for the $Zn_{(002)}$ coatings were higher than that for the $Zn_{(100)}$ coatings (39×10^{-4} mm^3 N^{-1} m^{-1}).

Ex situ analyses of wear track and counter body

The friction behavior observed in Fig. 5 can be explained with the help of the *ex situ* analyses of the third bodies on the counterface and the surfaces of the worn coatings. Fig. 6 shows the *ex situ* SEM micrographs of the counterfaces (top panel) and wear tracks (bottom panel) of the $Zn_{(100)}$ coating. Adhesive wear dominated the early sliding cycles. The presence of a thicker transfer film on the counter body after 10 cycles increased the COF from 0.3 to 0.8. At 200 cycles, a point in the test where the COF was relatively stable at 0.75, the transfer film on the counter surface was still present, but started to break apart and some parts spalled off from the surface. On the coating, the wear track widened and there was evidence of scattered wear debris within the track. At 500 cycles the friction momentarily decreased to 0.4 and then increased to 0.6. At this stage, most of the transfer film was removed, with some thinner transfer film in the center and scattered loosely adhered granular white debris on the sides, indicative of oxidational wear. The effective contact area on the counter surface also increased. With an increase in sliding cycles, the granular materials present on the track redeposited onto the surface of the ball. This kind of transfer film rheology has been well documented in these kinds of coatings using an *in situ* tribology technique.[11] At 850 cycles, the counter surface was devoid of any transfer film in the center, with accumulated third bodies on the side accompanied by further increases in contact area. Detailed chemical analysis of the debris and transfer films was conducted to understand the wear mechanism.

Fig. 7 shows the *ex situ* SEM micrographs of the $Zn_{(002)}$ coating. In the early stages, the formation of a thick transfer

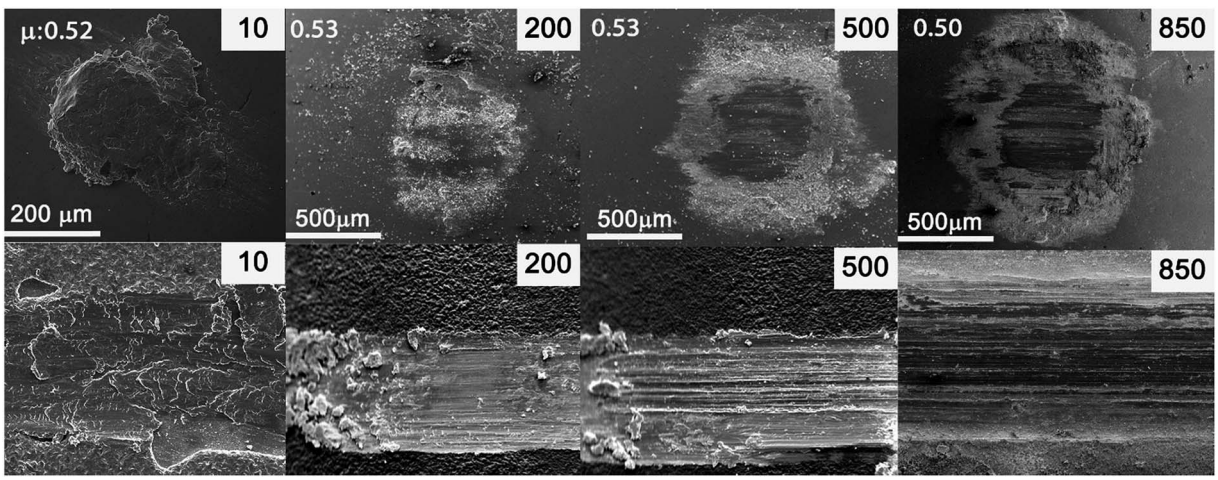

Fig. 7 *Ex situ* SEM micrographs of the counterface (top) and wear track (bottom) of $Zn_{(002)}$ coatings.

film accompanied by an increase in friction was similar to that seen for the $Zn_{(100)}$ coating. However, as shown in Fig. 5a, the increase in friction was only to 0.52, whereas for the $Zn_{(100)}$ coating it was to 0.7. Clear differences were also observed for the *ex situ* analysis at cycle 10, where a wide wear track and an accompanying wide transfer film formed on the counter surface. The wear track for $Zn_{(002)}$ also showed a fishscale-type morphology suggestive of adhesive wear. The softer $Zn_{(002)}$ coating showed much more wear in the early cycles than the $Zn_{(100)}$ coating (Fig. 5b). In addition to the mechanical properties, the dominant factor in the wear of this coating was the orientation of the basal plane. The basal plane was parallel to the sliding direction in the $Zn_{(002)}$ coating. In this configuration, lower shear stresses were sufficient to induce basal cleavage and hence larger wear at a lower level of friction. The observed wear rates were in good agreement with previously reported data for electrodeposited Zn on copper substrates.[25] The $Zn_{(002)}$ exhibited a loss of transfer material on the counter surface at 200 cycles and white granular debris started to appear. At 500 cycles the contact area on the counter surface increased, with a compact transfer film on the circumference. At 850 cycles there was minimal accumulation of a transfer film in the center of the contact. The wear track showed the formation of a dark layer with a minimum amount of coating adhering to the surface. The composition of this tribo layer was studied in detail by spectral analyses.

Crystallographic orientations and mechanical properties of the wear tracks

Fig. 8 shows the orientation of the $Zn_{(100)}$ and $Zn_{(002)}$ wear tracks as a function sliding cycle. The orientation of the $Zn_{(100)}$ wear track (Fig. 8) remained the same as that of the unworn coating until 200 cycles. The (100) fibers began to spread along the rolling direction (sliding direction) at 500 cycles, showing a transformation in the orientation of the wear track. The pole figures measured on the wear track after 2000 cycles had a non-fiber (100) orientation, which is different from the original coating orientation, as a consequence of Zn on the steel grains. This change in orientation is due to extensive plastic deformation during the wear test. In contrast, no change was observed on the (110) planes during wear, except that the planes changed from fiber to non-fiber orientations with reduced intensities. The transfer film layer orientation on $Zn_{(002)}$ (Fig. 8) showed a different behavior from the $Zn_{(100)}$ coatings. The change in the basal fibers to non-fiber orientations occurred quickly within 100 cycles. As the wear tests progressed to 200 cycles, the non-fiber orientation of the Zn basal planes was characterized by the appearance of two maxima in the pole figures. Above 500 cycles, the coating orientation was mixed fiber and non-fiber; this could be due to the drastic reduction in thickness and loss of coating volume. Most of the tribo layers left on the wear track were mixed oxides.

The electrodeposited $Zn_{(100)}$ and $Zn_{(002)}$ coatings showed different run-in behaviors. Up to 450 cycles, the $Zn_{(100)}$ coating showed higher friction. The mechanical properties of the wear tracks generated at different sliding cycles were studied at different locations on the wear tracks by nanoindentation. Fig. 9a and b compare the wear track hardness and variation in modulus as a function of sliding cycle for the $Zn_{(100)}$ and $Zn_{(002)}$ coatings, respectively. There was no significant increase in hardness for the $Zn_{(100)}$ wear track up to 50 cycles and the values were comparable with those of the as-deposited coating (Fig. 4); however, the hardness increased from 1.2 to 1.8 GPa at 100 cycles. From 100 to 500 cycles the hardness began to decrease to

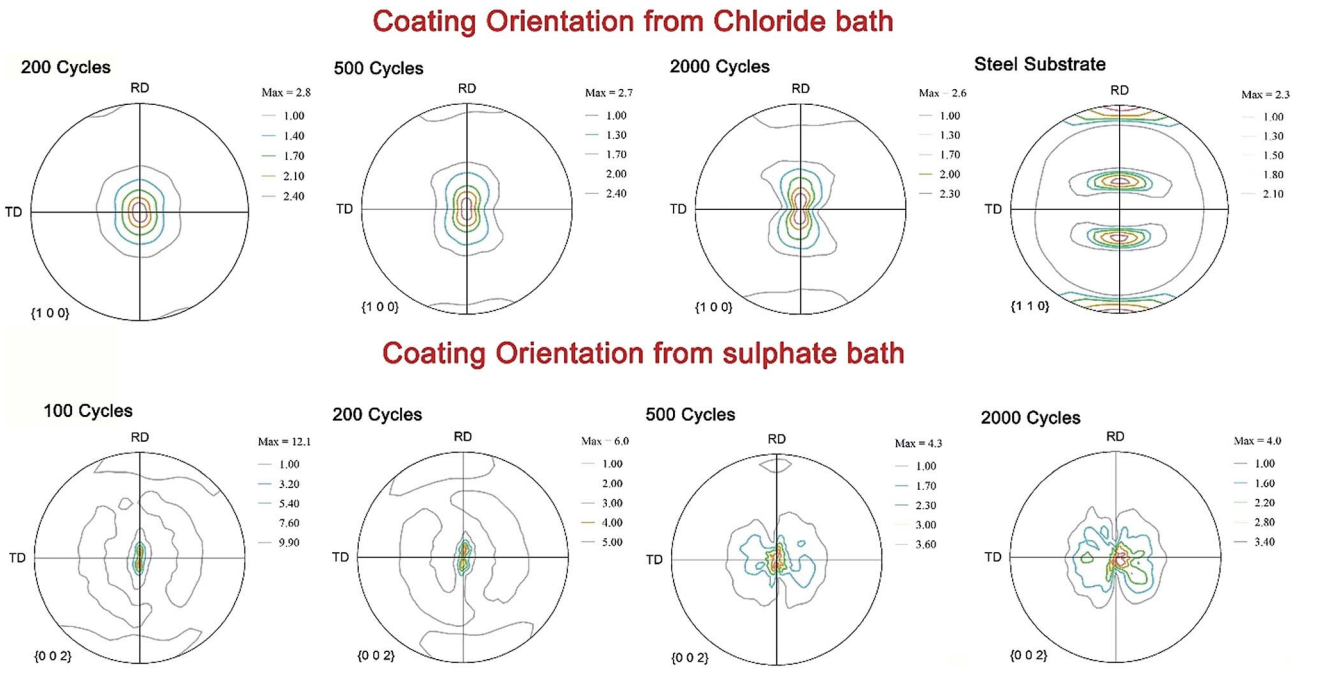

Fig. 8 Coating orientations on the track after the wear test.

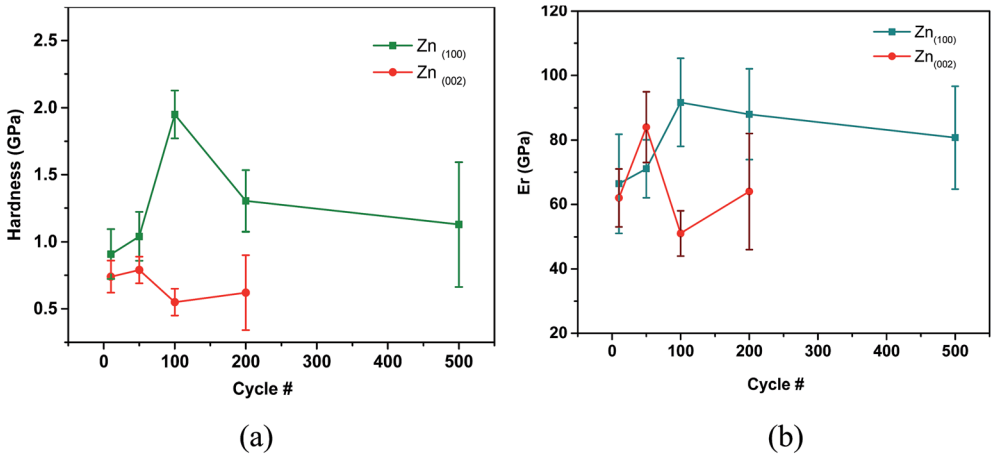

Fig. 9 Mechanical properties on the wear track with respect to number of cycles: (a) hardness *versus* cycle number; and (b) reduced modulus *versus* cycle number.

a value similar to that of the unworn coating. In contrast, the $Zn_{(002)}$ wear tracks did not show a significant increase in hardness, although the influence of the substrate was observed on the measured hardness at 500 cycles. From the *ex situ* analyses (Fig. 7), it was evident that most of the Zn coating was worn and that the steel on the steel contact started to dominate after 500 cycles.

The observed increase in hardness for the $Zn_{(100)}$ coating during the initial 100 cycles was a result of sliding-induced strain hardening. At the early stages of sliding, the $Zn_{(100)}$ tracks had elongated patches. A cyclic indentation was performed on the elongated patches (Fig. 10) in addition to the wear track to check for indentation-induced strain hardening. Fig. 10 shows the load displacement curve obtained from the cyclic indent. The deformed patches showed higher hardness compared with the undeformed wear track region. No significant increase in hardness was observed as a result of cyclic loading.

The *c*-axis is parallel to the sliding direction in $Zn_{(100)}$. This is a very well-established phenomenon for Zn and the deformation in the *c*-axis direction leads to strain hardening. The primary reason for hardening is the formation of dislocation dipoles arising during the intersection of dislocations traveling in any one of the $(11\bar{2}2)$ pyramidal planes.[26] During the early stages (10 cycles) of sliding only few elongated patches on the wear track showed increased hardness. Fig. 10 shows the load displacement curves generated from a partial unloading indentation experiment performed on two regions on the wear track. The SEM micrograph of the indent is also shown. Indentation performed on the elongated patch showed a higher hardness (1.8 GPa) at depths <30 nm. The hardness decreased to a value similar to that of the as-deposited coating (~1 GPa) with an increase in contact depth, although indentation performed on the adjacent track region showed no change in hardness with contact depth. From 10 to 100 cycles the contact conditions remained the same and the counter ball surface had a thicker transfer film (Fig. 6). The transfer film started to break at >200 cycles and the removal of the strain-hardened layer decreased the wear track hardness from 1.8 to 1.2 GPa. At 500 cycles, the presence of oxides and the rough wear track produced larger scattering.

Chemical analysis of the wear track

Energy-dispersive X-ray spectrometry was carried out on the wear track and transfer films (ball surface). Traces of oxide were detected on ball and wear track (not shown) surfaces for both the $Zn_{(100)}$ and $Zn_{(002)}$ coatings at higher sliding cycles (>100). Fig. 11a shows representative SEM micrographs of the third bodies (from $Zn_{(100)}$) and Fig. 11b shows the corresponding EDS spectra. The debris was predominantly Zn at <50 cycles.

At higher cycles, both Fe and Zn peaks were detected, together with oxygen. It was difficult to determine whether the oxides formed were Zn, Fe, or a mixture of both. Li *et al.*[15] previously showed the transition from adhesive wear to oxidative wear in electrodeposited Zn coatings. To understand the

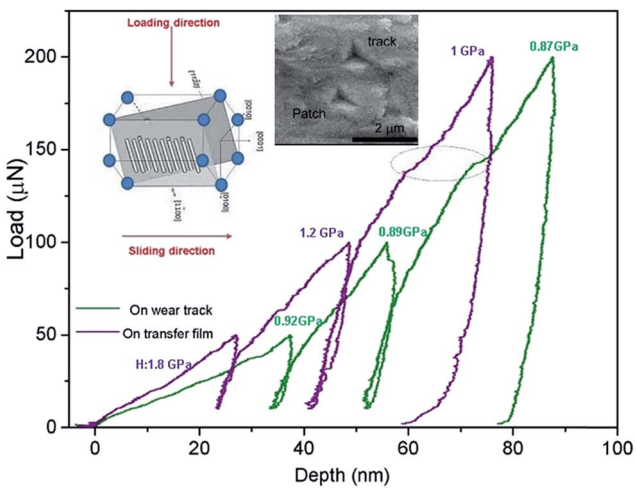

Fig. 10 Load displacement curve and corresponding SEM micrograph of the indents obtained from the cyclic indentation on two regions of the wear track of the $Zn_{(100)}$ coating.

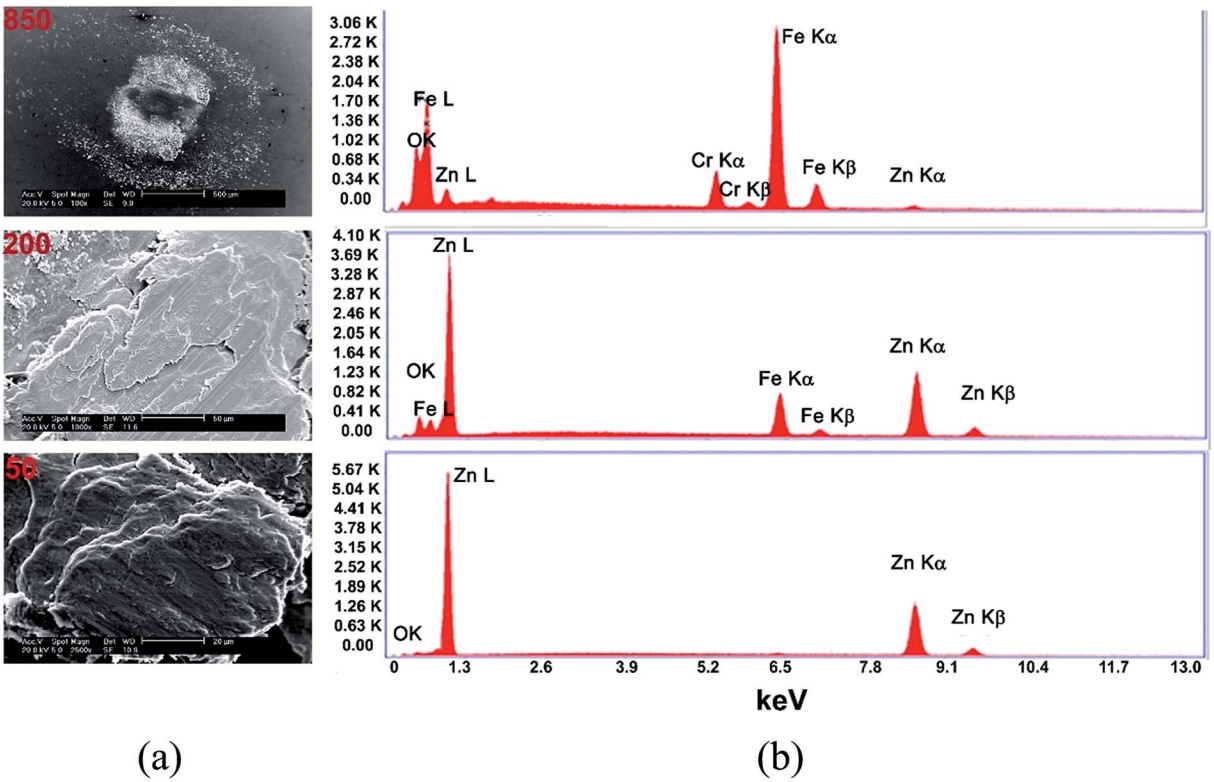

Fig. 11 (a) Representative SEM micrograph of the transfer film on the ball surface for $Zn_{(100)}$. (b) EDS spectra showing the presence of oxide.

chemical process involved during the transition from adhesive to oxidative wear, the transfer films and wear tracks were analyzed using Raman spectrometry. Fig. 12 and 13 show the Raman spectra recorded from the wear track and ball surfaces for the two coatings.

In the $Zn_{(100)}$ coating, only one noticeable peak was observed at 555 cm^{-1} up to 100 cycles for the wear track and counter face (Fig. 12). The EDS analysis confirmed that the debris at lower sliding cycles was rich in Zn and the most probable candidate at this stage was ZnO. The 555 cm^{-1} peak was attributed to the A_1 longitudinal optical (LO) phonon mode of wurtzite.[27,28] In this study, we did not observe any peak corresponding to the E_2 (low or high), A_1 transverse optical (TO), E_1 (TO) or E_1 (LO) phonon modes. As the Zn coatings had a strong texture, an ordered oxide film was expected. For ordered ZnO films in the back-scattered Raman geometry, only A_1 (LO) and E_2 modes were expected.[27] At 200 cycles, a single peak was observed at 657 cm^{-1} corresponding to a mixture of Fe oxide and Zn oxide.[29,30] At 500 cycles the wear track contained a mixed oxide, whereas the debris showed stronger Zn oxide bands. Fe oxide dominated the composition at higher numbers of cycles (>500). For the $Zn_{(002)}$ coatings (Fig. 13), ordered Zn oxide was only detected at 200 cycles. Wear tracks obtained at ≥500 cycles showed stronger iron oxide peaks.[31–33]

The experimental data (EDS and Raman) for the chemical nature of the mixed oxides were further corroborated by thermodynamic calculations. The calculations were performed using the thermodynamic software Factsage[34] and the FToxide database. Fig. 14 shows that a ZnO phase is expected at 25 °C and an atmospheric concentration of oxygen for pure Zn, whereas a mixture of zincite ($ZnO + Fe_3O_4$) and spinel ($ZnFe_2O_4 + Fe_3O_4$) is possible in an Fe–Zn–O system under the same conditions.

Fig. 15 is a schematic diagram showing the sequence of the wear process for the $Zn_{(100)}$ and $Zn_{(002)}$ coatings. Three different stages were identified for $Zn_{(100)}$: (1) transfer film formation and strain hardening; (2) transfer film removal from the ball surface and oxidation of the counter surface; and (3) the formation of an Fe oxide and Zn oxide mixture followed by steady-state friction. For $Zn_{(002)}$, the sequences in the wear process were: (1) steady removal of material with some transfer film formation in the early stage; (2) direct contact of the steel ball–steel substrate resulting in Fe oxide on both the ball and track surface; and (3) oxidation of the Zn debris followed by steady-state friction.

Although both coatings showed the presence of lubricious oxides, they originated from two different scenarios. For the $Zn_{(100)}$ system, most of the coating was intact throughout the test and the Fe oxide peak was first detected on the ball surface (Fig. 12b, 200 cycles). Thicker black oxide debris was observed on the ball surface at 500 cycles (Fig. 12c, 500 cycles). Above 500 cycles, granular oxide debris entered the sliding contact and smearing of the oxide debris resulted in an increase in friction (Fig. 5a, 500–750 cycles). Once a smooth transfer film had formed on the ball surface, the friction started to stabilize. The optical micrograph of the ball surface at 850 and 1200 cycles showed smooth patches of Fe oxide covering the majority of the

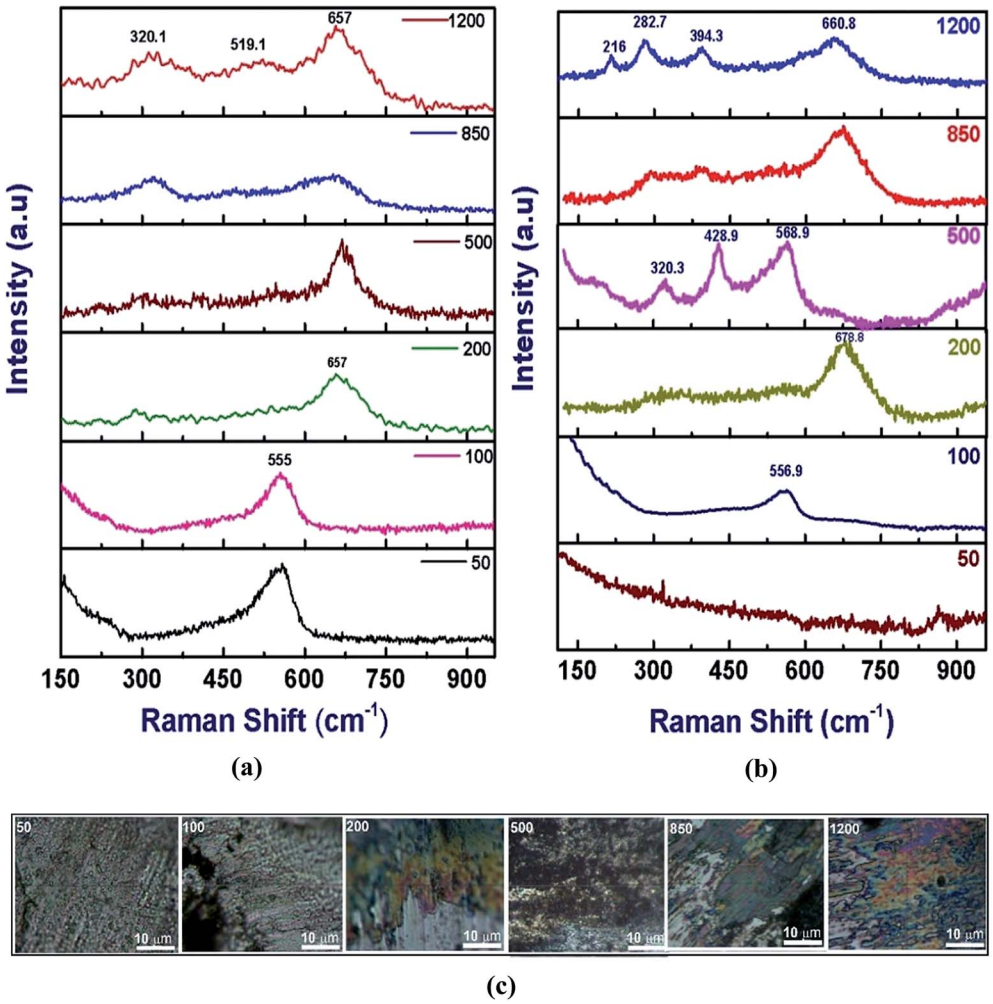

Fig. 12 Raman spectra from $Zn_{(100)}$: (a) from the wear track surface; and (b) from the ball surface. (c) Optical images of the transfer film.

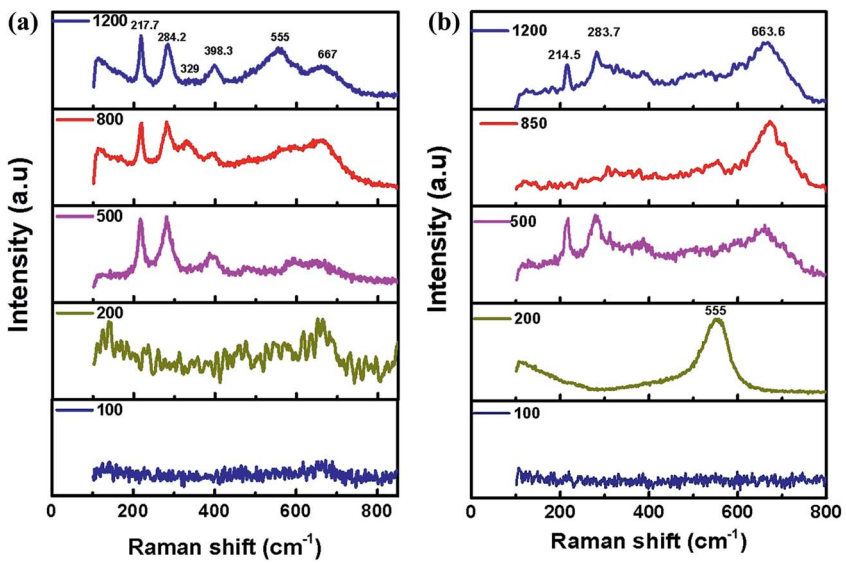

Fig. 13 Raman spectra from the wear track of $Zn_{(002)}$: (a) from the wear track surface; and (b) from the ball surface.

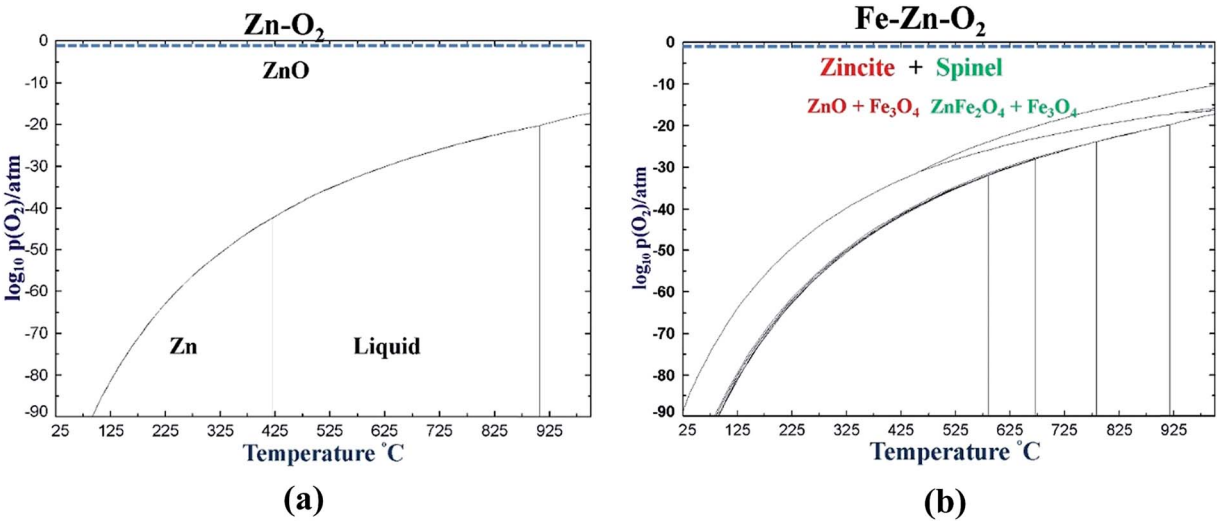

Fig. 14 (a) Binary phase diagram of Zn–O system. (b) Ternary phase diagram of the Fe–Zn–O system.

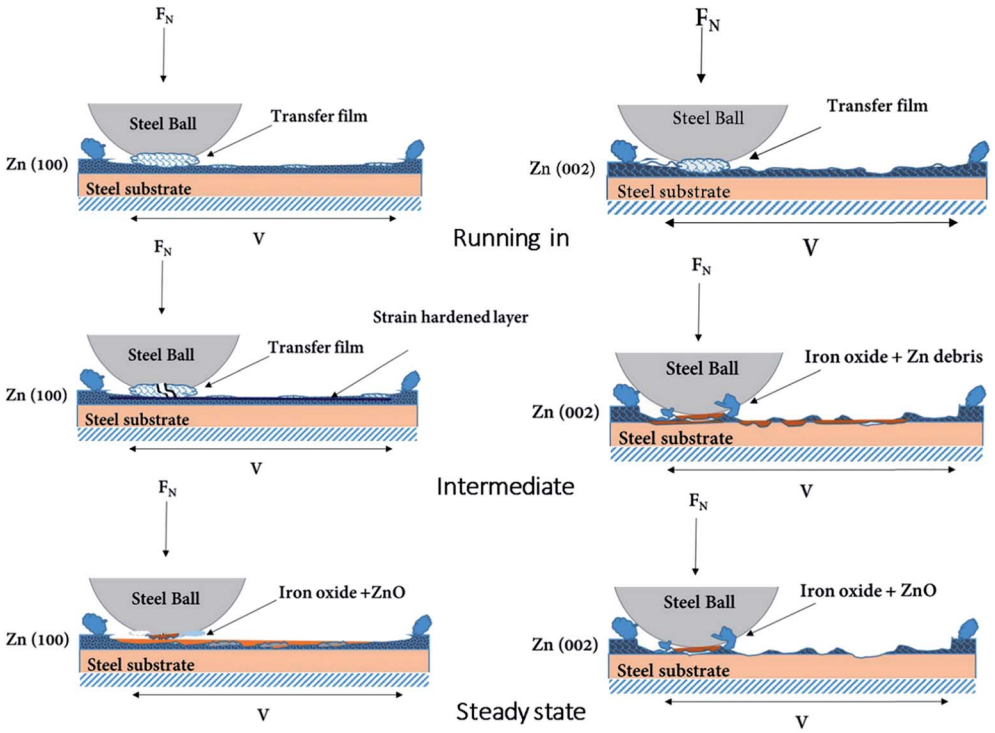

Fig. 15 Schematic diagram of the wear behavior of the $Zn_{(100)}$ and $Zn_{(002)}$ coatings.

contact area. The sliding of oxide transfer film (on the ball surface) against the Fe oxide and Zn oxide patches on the wear track resulted in steady-state friction. For the $Zn_{(002)}$ coating, most of the coating was consumed by the wear process before steady-state friction and direct rubbing of the steel ball against the steel substrate produced Fe oxide and redeposited oxide films dominated the steady-state friction regime.

Both $Zn_{(100)}$ and $Zn_{(002)}$ showed similar steady-state friction. However, at the end of wear test most of the $Zn_{(002)}$ coating was consumed and the steady-state friction came from lubricious oxide films,[27] not from the original coating. However, the $Zn_{(100)}$ coating showed superior wear characteristics. For Zn protective coatings, it is not the low shear strength, but rather the higher hardness and naturally formed ZnO that determines the wear characteristics.

Conclusions

The tribological behavior of coatings with different preferred orientations was observed to be different. The initial peak

friction and the run-in behavior were higher for the $Zn_{(100)}$ coating than for the $Zn_{(002)}$ coating. Both coatings showed the formation of transfer films during the run-in period. The steady-state friction after the run-in behavior was also observed to be same, except that the $Zn_{(100)}$ coating showed some instability. The wear rate of the $Zn_{(100)}$ coating was less than that of the $Zn_{(002)}$ coating. Mixed-mode oxidation was observed in the steady-state friction regime for both coatings, but the onset of Fe oxide formation was earlier in the $Zn_{(002)}$ coating. From the point of view of tribological applications, harder Zn $_{(100)}$ coatings with naturally formed or reactively formed ZnO layers are preferable to softer $Zn_{(002)}$ coatings with dominant basal slip.

Acknowledgements

The authors thank Dr Manas Paliwal for his help with the thermodynamic calculations. Ms Lisa Lee and Mr Priyadarshi Behera are acknowledged for their support in the experiments. Mr Salim Brahmi's technical input regarding industrial plating operations is also acknowledged. The authors thank the Natural Sciences and Engineering Council of Canada (NSERC) and industrial partners Pratt & Whitney Canada, Messier Bugatti Dowty Canada, and Heroux-Devtek for their financial support and engineering input.

References

1 R. Winand, in *Modern Electroplating*, John Wiley & Sons, Inc., 2010, pp. 285–307, DOI: 10.1002/9780470602638.ch10.
2 I. Tomov, C. Cvetkova, V. Velinov, A. Riesenkampf and B. Pawlik, *J. Appl. Electrochem.*, 1989, **19**, 377–382.
3 M. Mouanga, L. Ricq, G. Douglade, J. Douglade and P. Berçot, *Surf. Coat. Technol.*, 2006, **201**, 762–767.
4 M. Mouanga, L. Ricq, J. Douglade and P. Berçot, *J. Appl. Electrochem.*, 2007, **37**, 283–289.
5 K. Raeissi, M. R. Bateni, A. Saatchi, M. A. Golozar and J. A. Szpunar, *Surf. Coat. Technol.*, 2006, **201**, 3116–3122.
6 K. Raeissi, A. Saatchi and M. A. Golozar, *J. Appl. Electrochem.*, 2003, **33**, 635–642.
7 K. Raeissi, A. Saatchi, M. A. Golozar and J. A. Szpunar, *J. Appl. Electrochem.*, 2004, **34**, 1249–1258.
8 K. Raeissi, A. Saatchi, M. A. Golozar and J. A. Szpunar, *Surf. Coat. Technol.*, 2005, **197**, 229–237.
9 ASTM-F1941-00, Journal, DOI: 10.1520/F1941-07.
10 K. R. Sriraman, H. W. Strauss, S. Brahimi, R. R. Chromik, J. A. Szpunar, J. H. Osborne and S. Yue, *Tribol. Int.*, 2012, **56**, 107–120.
11 K. R. Sriraman, S. Brahimi, J. A. Szpunar, J. H. Osborne and S. Yue, *Electrochim. Acta*, 2013, **105**, 314–323.
12 K. R. Sriraman, S. Brahimi, J. A. Szpunar and S. Yue, *J. Appl. Electrochem.*, 2013, **43**, 441–451.
13 Q. Li, Z. Feng, J. Zhang, P. Yang, F. Li and M. An, *RSC Adv.*, 2014, **4**, 52562–52570.
14 Q. Li, Z. Feng, L. Liu, H. Xu, W. Ge, F. Li and M. An, *RSC Adv.*, 2015, **5**, 32479–32490.
15 Q. Li, Z. Feng, L. Liu, J. Sun, Y. Qu, F. Li and M. An, *RSC Adv.*, 2015, **5**, 12025–12033.
16 J. Giridhar and W. J. van Ooij, *Surf. Coat. Technol.*, 1992, **53**, 35–47.
17 A. C. Hegde, K. Venkatakrishna and N. Eliaz, *Surf. Coat. Technol.*, 2010, **205**, 2031–2041.
18 H. W. Strauss, R. R. Chromik, S. Hassani and J. E. Klemberg-Sapieha, *Wear*, 2011, **272**, 133–148.
19 R. R. Chromik, H. W. Strauss and T. W. Scharf, *JOM*, 2012, **64**, 35–43.
20 K. J. Wahl and I. L. Singer, *Tribol. Lett.*, 1995, **1**, 59–66.
21 W. C. Oliver and G. M. Pharr, *J. Mater. Res.*, 1992, **7**, 1564–1583.
22 G. M. Pharr and W. C. Oliver, *MRS Bull.*, 1992, **17**, 28–33.
23 L. E. Morón, A. Méndez, F. Castañeda, J. G. Flores, L. Ortiz-Frade, Y. Meas and G. Trejo, *Surf. Coat. Technol.*, 2011, **205**, 4985–4992.
24 R. Parisot, S. Forest, A. Pineau, F. Grillon, X. Demonet and J.-M. Mataigne, *Metall. Mater. Trans. A*, 2004, **35**, 797–811.
25 C. N. Panagopoulos, K. G. Georgarakis and S. Petroutzakou, *J. Mater. Process. Technol.*, 2005, **160**, 234–244.
26 A. Nazeer, PhD thesis, California Institute of Technology, 1965.
27 J. S. Zabinski, J. Corneille, S. V. Prasad, N. T. Mc Devitt and J. B. Bultman, *J. Mater. Sci.*, 1997, **32**, 5313–5319.
28 K. A. Alim, V. A. Fonoberov, M. Shamsa and A. A. Balandin, *J. Appl. Phys.*, 2005, **97**, 124313.
29 Q. Tian, Q. Wang, Q. Xie and J. Li, *Nanoscale Res. Lett.*, 2010, **5**, 1518–1523.
30 I. G. Aksyanov, M. E. Kompan, I. V. Kul'kova and Y. P. Stepanov, *Glass Phys. Chem.*, 2012, **38**, 143–148.
31 S. Oh, D. C. Cook and H. E. Townsend, *Hyperfine Interact.*, 1998, **112**, 59–66.
32 S.-H. Shim and T. S. Duffy, *Am. Mineral.*, 2002, **87**, 318–326.
33 O. N. Shebanova and P. Lazor, *J. Raman Spectrosc.*, 2003, **34**, 845–852.
34 C. W. Bale, E. Bélisle, P. Chartrand, S. A. Decterov, G. Eriksson, K. Hack, I. H. Jung, Y. B. Kang, J. Melançon, A. D. Pelton, C. Robelin and S. Petersen, *Calphad*, 2009, **33**, 295–311.

